Clarifying the local structure of dopants in garnet solid-state electrolytes for lithium-ion batteries

Sundeep Vema[1,2], Astrid H. Berge[1], Supreeth Nagendran[1], Clare P. Grey[1,*]

[1] Yusuf Hamied Department of Chemistry, University of Cambridge, Lensfield Road, Cambridge, CB2 1EW, United Kingdom

[2] The Faraday Institution, Quad One, Harwell Campus, Didcot, OX11 0RA, United Kingdom

Corresponding Author

[*] Clare P. Grey – Yusuf Hamied Department of Chemistry, University of Cambridge, Lensfield Road, CB2 1EW Cambridge, United Kingdom; The Faraday Institution, Quad One, Harwell Campus, Didcot, OX11 0RA, United Kingdom; orcid.org/0000-0001-5572-192X; Email: cpg27@cam.ac.uk

Abstract

The high Li-ion conductivity and wide electrochemical stability of Li-rich garnets ($Li_7La_3Zr_2O_{12}$) make them one of the leading solid electrolyte candidates for solid-state batteries. Dopants such as Al and Ga are typically used to enable stabilisation of the high Li^+ ion-conductive cubic phase at room temperature. Although numerous studies exist that have characterized the electrochemical properties, structure, and lithium diffusion in Al- and Ga-LLZO, the local structure and site occupancy of dopants in these compounds are not well understood. Two broad ^{27}Al or $^{69,71}Ga$ resonances are often observed with chemical shifts consistent with tetrahedrally coordinated Al/Ga in the magic angle spinning nuclear magnetic resonance (MAS-NMR) spectra of both Al- and Ga-LLZO, which have been assigned to either Al and/or Ga occupying 24d and 96h/48g sites in the LLZO lattice or to the different Al/Ga configurations that arise from different arrangements of Li around these dopants. In this work, we unambiguously show that the side products γ-$LiAlO_2$ and $LiGaO_2$ lead to the high frequency resonance observed by NMR spectroscopy and that both Al and Ga only occupy the 24d site in the LLZO lattice. Furthermore, it was observed that the excess Li often used during synthesis leads to the formation of these side-products by consuming the Al/Ga dopants. In addition, the consumption of Al/Ga dopants lead to the tetragonal phase formation commonly observed in the literature even after careful mixing of precursors. The side-products can exist even after sintering, thus controlling the Al/Ga content in the LLZO lattice, substantially influencing the lithium-ion conductivity in LLZO as measured here by electrochemical impedance spectroscopy.

1. Introduction

Solid-state batteries have been projected to enable energy storage devices with higher energy density and thermal stability than current, state-of-the-art organic liquid electrolyte-based batteries[1,2]. A solid electrolyte is the key component of a solid-state battery that enables these features and consequently a wide range of lithium containing inorganic oxides, sulphides and nitrides have been explored as solid electrolytes. Li-rich garnets ($Li_7La_3Zr_2O_{12}$, LLZO) possess high room temperature (RT) ionic conductivity and relatively wide electrochemical stability as compared to other solid electrolytes and have therefore been a subject of intense interest in the past few years[3].

LLZO with cubic $Ia\bar{3}d$ symmetry was synthesised at 1230 °C by Murugan *et al.*[4] for the first time in 2007 and was shown to have the highest RT ionic conductivity (~ 3×10^{-4} Scm^{-1}) with a low activation energy of 0.3 eV. However, Awaka *et al.*[5] reported that LLZO synthesised at 900 °C crystallises in a tetragonal structure, $I4_1/acd$, through single crystal and powder X-ray diffraction (XRD) and neutron diffraction. A relatively low ionic conductivity (~ 10^{-6} Scm^{-1}) with a high activation energy (0.54 eV) was also reported. A follow up study on single crystals of LLZO synthesised at 1250 °C noted the formation of cubic LLZO where Li occupied a combination of tetrahedral sites (24d) and distorted octahedral sites (96h)[6]. In a high temperature XRD study performed on $Li_7La_3Sn_2O_{12}$, a compound with a similar structure to LLZO, Percival *et al.*[7] observed the transformation from a tetragonal to a cubic unit cell above 750 °C but the compound transformed back to tetragonal on cooling to RT. It was hypothesised that LLZO synthesised at high temperatures (above 1200 °C) might result in disordered structures that could be stabilised by Li loss during cooling to form cubic $Li_{7-x}La_3Zr_2O_{12-x/2}$.

Through a systematic study of LLZO synthesis at 900-1100°C in two crucibles, Al_2O_3 and platinum, Geiger *et al.*[8] revealed the origin of cubic LLZO. They showed that a small amount of aluminium from the Al_2O_3 crucible was incorporated into the LLZO lattice leading to the transformation from a tetragonal to cubic structure. Consistent with this, such a transformation was not observed in LLZO synthesised in platinum crucibles. These observations were supported by using a range of techniques, including electron probe microanalysis, laser ablation inductively coupled plasma mass spectrometry and ^{27}Al MAS NMR spectroscopy. The aluminium-induced cubic transformation of LLZO was subsequently confirmed by intentional addition of Al_2O_3 during synthesis in later studies[9–12].

These observations suggested that Li content reduction in the LLZO framework through multivalent dopants could lead to the stabilisation of the highly conductive cubic lattice and thus, different combinations of dopants (Al, Ga, Fe, Ta, W, Nb etc.) have been explored to stabilise the cubic polymorph of LLZO and to obtain high Li-ion conductivities[13–18]. Among various doped LLZO compounds reported in the literature, Al doped LLZO (Al-LLZO) and Ga doped LLZO (Ga-LLZO) have high RT ionic conductivity (~10^{-4} and 10^{-3} Scm^{-1} respectively) making them promising candidates for commercial applications. Although numerous studies exist that have characterized the electrochemical properties[19,20], structure[19,21,22] and nature of lithium diffusion in Al- and Ga-LLZO[23–31], the nature of the local structure, and the site occupancy of the dopants is still unclear.

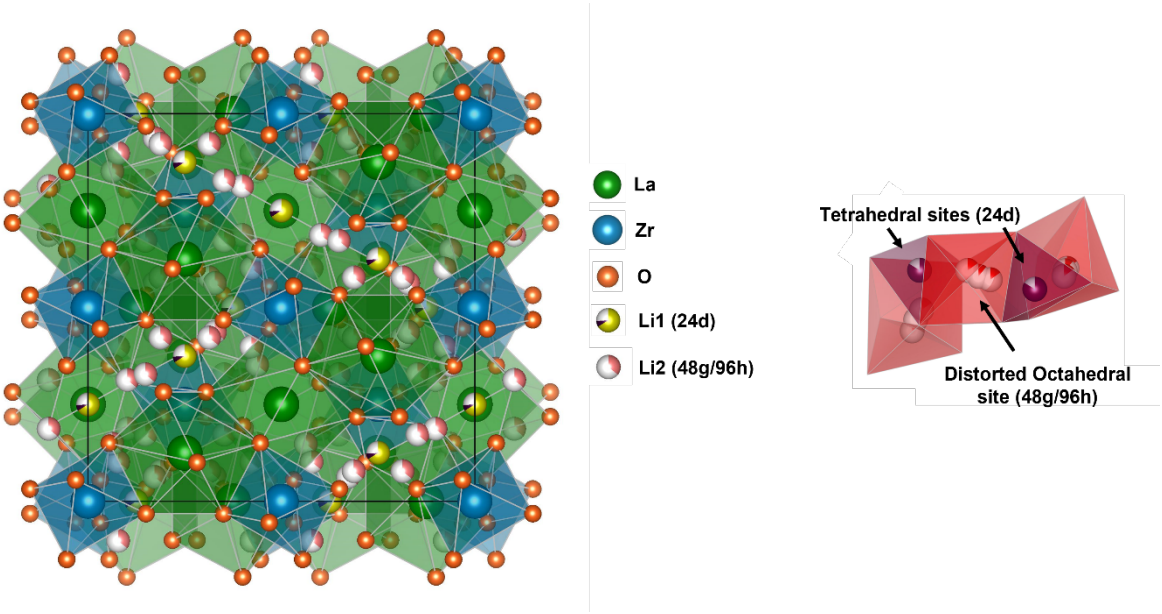

Figure 1: Crystal structure of cubic Al-LLZO (Space group $Ia\bar{3}d$) in z direction. Li1 site can be occupied by both Li^{+} and Al^{3+}. The structure has been generated with VESTA 3.4.7[32]. Representation of interconnected Li network in Al-LLZO, where the Li1 tetrahedral sites (24d) and the Li2 distorted octahedral sites (48g/96h) are connected by face sharing tetrahedra/octahedra and both these sites have been reported as possible occupancy sites for Al/Ga.

One of the earliest studies investigating the local structure of Al in Al-LLZO was performed by Geiger *et al.*[8] who reported that Al occupies two distinct sites in LLZO based on the two different signals observed in the tetrahedral region of the ^{27}Al MAS NMR spectrum of Al-LLZO powder collected at 9.4 T. The signal at ~ 68 ppm was assigned to Al in a tetrahedral site (24d) and the signal at ~ 81 ppm to a distorted octahedral site (96h), which has an approximate 5-fold coordination environment (Figure 1). Buschmann *et al.*[33] and Kuhn *et al.*[34] assigned the higher shifted resonance in ^{27}Al MAS NMR spectrum to Al^{3+} in tetrahedral sites adjacent to La^{3+} or Zr^{4+} vacancies. In a different study by Düvel *et al.*[35], a series of Al-LLZO

compounds were prepared with increasing Al^{3+} contents via high energy mechanical milling followed by annealing at 600 °C and ^{27}Al MAS NMR spectra of the compounds were measured. Multiple resonances were observed in addition to the two resonances discussed above, which were attributed to Al^{3+} occupation of either La^{3+} or Zr^{4+} sites in the LLZO lattice. Rettenwander *et al.*[36] performed DFT calculations to determine the origin of the two resonances seen in ^{27}Al MAS NMR spectra and proposed that Al^{3+} occupied both tetrahedral (24d) and 4-fold coordinated distorted octahedral (96h) sites based on the similar calculated energies for Al^{3+} occupation of the sites. Small displacements of Al^{3+} ions were observed to lead to a distribution of different local oxygen coordination environments, and this was hypothesised as a reason for the existence of broad resonances in the ^{27}Al MAS NMR spectra. In a further high-field MAS NMR study performed on $Al_xGa_yLi_{7-3(x+y)}La_3Zr_2O_{12}$ solid solutions by Rettenwander *et al.*[37], the existence of two Al^{3+} environments in Al-LLZO powder was confirmed and these were attributed to the two sites in LLZO lattice as reported earlier. Similar observations have been made by high-resolution synchrotron XRD (SXRD), Neutron powder diffraction and Raman spectroscopy performed on Al-LLZO powder[38–40]. In a recent study by some of us, through a combination of DFT and MAS NMR experiments, Karasulu and Emge *et al.*[41] argued that Al^{3+} occupancy of distorted octahedral site (96h) was energetically unfavourable and proposed that differences in the number of Li ions adjacent (i.e., in the first cation coordination shell) to the Al^{3+} dopant could lead to a series of different configurations, accounting for the different resonances seen in ^{27}Al MAS NMR spectrum of Al-LLZO. Similar discussions exist concerning the occupancies of Ga^{3+} in LLZO are also present in the literature[41–45].

In this work, a systematic investigation of the local structure of the Al dopant in Al-LLZO and Ga dopant in Ga-LLZO with ^{27}Al and ^{71}Ga MAS NMR spectroscopy, respectively, was conducted on samples synthesised with differing amounts of Li excess in the precursors and on pellets sintered to produce particles with different grain sizes. Three different ^{27}Al resonances corresponding to two tetrahedral and one octahedral Al environment were observed in the ^{27}Al MAS NMR spectrum of Al-LLZO and two different ^{71}Ga resonances corresponding to two tetrahedral environments were observed in the ^{71}Ga MAS NMR spectrum of Ga-LLZO, as observed in earlier studies. Through MAS NMR performed on model compounds and by double quantum – single quantum (DQ-SQ) correlation experiments, it was confirmed that the dopants occupy only one crystallographic site in both Al- and Ga-LLZO and all other additional resonances were due to the side-products present in samples. It was further found that a

significant amount of dopant can exist in side-products depending on the synthesis and sintering route. Electrochemical impedance spectroscopy (EIS) performed on different sintered samples showed that the dopant distribution between the side-products and LLZO lattice substantially influences the lithium-ion conductivity in LLZO solid electrolytes.

2. Experimental methods

2.1. Synthesis of Al-LLZO and Ga-LLZO powders

Al-LLZO and Ga-LLZO were synthesised using a solid-state method with excess Li (Both for Al- and Ga-LLZO) and stoichiometric Li precursors (Only for Al-LLZO) in MgO crucibles to avoid unintentional Al doping as described in detail in a previous study[46]. The synthesised doped LLZO powders were transferred above 200 °C to a glovebox to prevent any reaction with moisture and stored in air-tight vials.

For preparing hot-pressed samples, Al-LLZO and Ga-LLZO powders were first ground and sieved and then hot-pressed at 1080 °C for 70-90 mins using a custom-built induction coil based uniaxial hot-press as described in detail in a previous study[46]. The hot-pressed cylinder was cut using a diamond disc and the pellets were hand-polished inside a glovebox. The pellets were then ground using an agate mortar-pestle and stored in glovebox. To achieve pellets with large grain sizes, hot-pressed Al-LLZO pellets were sintered under flowing oxygen at 1200 °C for 18 hours. The pellets were centred on a flat MgO crucible cap and surrounded by a bed of synthesised Al-LLZO powder to avoid Li loss during sintering.

2.2. Synthesis of γ-$LiAlO_2$, $LiGaO_2$ and $LiAl_{0.5}Ga_{0.5}O_2$ powders

Al_2O_3 (TEM <50 nm, Sigma Aldrich) and Ga_2O_3 (99.999%, Alfa Aesar) were dried at 900 °C for 12 hours and transferred above 250 °C to a desiccator to allow them to cool down to RT. Li_2CO_3 (99.997%, Alfa Aesar) was dried at 150 °C for 12 hours. Precursors corresponding to 2 gm of γ-$LiAlO_2$, $LiGaO_2$ and $LiAl_{0.5}Ga_{0.5}O_2$ were stoichiometrically weighed and mixed for 20 mins in a mortar and pestle with acetone solvent to ensure homogeneous mixing. The solvent was then evaporated, and the dried powder was calcined at 1000 °C for 6 hours under O_2 flow, ~30 mL/min with a 5 °C/min heating rate in a tube furnace (Carbolite) followed by natural cooling. Al_2O_3 crucibles (SRX61, Almath crucibles) were used for the synthesis of γ-$LiAlO_2$ whereas MgO crucibles (SRX61MGO, Almath crucibles) were used for the synthesis of $LiGaO_2$ and $LiAl_{0.5}Ga_{0.5}O_2$ to prevent any unintentional incorporation of aluminium into the powder. The synthesised powders were transferred around 100 °C to a desiccator and stored in airtight vials for further analysis.

2.3. X-ray diffraction

The phase purity was confirmed by powder SXRD. Al-LLZO, γ-$LiAlO_2$, $LiGaO_2$, and $LiAl_{0.5}Ga_{0.5}O_2$ powders were finely ground in a mortar and pestle, filled in capillaries, and sealed using epoxy. Al-LLZO and Ga-LLZO samples were ground and packed inside the glovebox to prevent any reaction with moisture in the air. The capillaries were then transported

to the I11 beamline at the Diamond Light Source, Oxford, United Kingdom and SXRD patterns were collected at RT in transmission mode (λ = 0.824978 Å or 0.49381 Å). The transmitted X-rays were detected by position sensitive detectors. The SXRD patterns were then analysed using FullProf Suite[47].

2.4. Magic angle spinning nuclear magnetic resonance spectroscopy

All samples were ground in agate mortars and packed into 1.3 mm or 4 mm ZrO_2 rotors. Al-LLZO and Ga-LLZO samples were packed inside the glovebox and the other samples (γ-$LiAlO_2$ and $LiGaO_2$) were packed outside in ambient atmosphere. ^{27}Al and ^{71}Ga MAS NMR spectra were acquired on 700 MHz (16.4 T) magnets with Avance III consoles using a Bruker 1.3 mm HXY probe. The MAS NMR experiments were performed at sample spinning speeds of 40 kHz for 1.3 mm rotors. One-pulse pulse programs with a small flip angle (~π/12 and π/4 for ^{27}Al and ^{71}Ga respectively) were used to collect the MAS NMR spectra. ~π/12 flip angle was used in case of ^{27}Al for quantitative MAS NMR measurements. Due to the low abundance of the ^{71}Ga nuclei, and hence low signal-to-noise ratio, a small flip angle and hence quantitative measurements could not be done for Ga-LLZO. Instead, π/4 flip angle was used to maximise the signal intensity. The spectra were then externally referenced against AlF_3 powder (–17 ppm) for ^{27}Al and $Ga(NO_3)_3$ powder dissolved in distilled water (0 ppm) for ^{71}Ga. These reference compounds were also used for pulse length optimization.

Two-dimensional (2D) – Double Quantum Single Quantum (DQ-SQ) experiments were performed on a 1 GHz (23.5 T) magnet with Avance NEO consoles using a Bruker 1.9 mm HX probe. These experiments were performed with samples in 1.9 mm rotors at a MAS speed of 42 kHz. The pulse optimisation was done on a 1:1 mixture of Al_2O_3 and γ-$LiAlO_2$. The DQ-SQ experiments were performed using the $BR2_2^1$ homonuclear recoupling sequence[48].

The MAS NMR spectra were processed and deconvoluted with Bruker Topspin 4.0.8 and dmfit software packages[49]. The ^{27}Al and ^{71}Ga MAS NMR spectra were fitted with the Q-MAS 1/2 model to fit the central transition assuming infinitely fast MAS to obtain values of the quadrupolar coupling (C_Q) and asymmetry parameter (η_Q).

2.5. Scanning electron microscopy

A Tescan MIRA3 FEG-SEM was used to collect the SEM images with 5 keV accelerating voltage and 6-8 mm working distance. The samples were sputter coated with platinum to reduce the charging effects during imaging. Energy dispersive x-ray spectroscopy (EDS) was performed on an Oxford Instruments X-maxN 80 EDS system. EDS was performed using an electron beam with 30 keV acceleration voltage and 15 mm working distance.

2.6. Impedance measurements

The polished pellets inside the glovebox were placed in a MgO crucible and transferred to a custom-made quartz tube and thermally etched in a furnace (Carbolite) with a custom-made gas setup to switch between argon and oxygen to remove the surface passivation layers[46]. The pellets were heated under O_2 at 500 °C for 1 hour at the rate of 10 °C/min and then cooled to

200 °C at 10 °C/min. The quartz tube was then purged with argon for 20 mins and then transferred at 200 °C into the glove-box pre-chamber. For blocking electrode measurements, the thermally etched pellets were centred under a stainless-steel disc having a 5 mm Ø hole, and sputter coated with gold on both sides of the pellets. Then the pellets were closed in Swagelok cells for further characterization. The impedance measurements were performed with an amplitude of 10 mV at frequencies from 7 MHz to 1 Hz using a VSP-300 (Biologic). The impedance data was fit with an equivalent circuit using a custom written code in Python to extract the bulk and grain boundary ionic conductivities.

3. Results and Discussion

3.1. MAS NMR of Al-LLZO and γ-$LiAlO_2$

Al-LLZO ($Al_{0.36}Li_{5.92}La_3Zr_2O_{12}$) was synthesised with 10% extra Li in the precursors (referred to as Al-LLZO +10%Li) and its high-resolution SXRD pattern is shown in Figure 2a. Rietveld refinement showed that the Al-LLZO +10%Li sample was composed of cubic Al-LLZO (~82%), tetragonal (Al)-LLZO (~15%) and side-products $LaAlO_3$ (~2%) and Li_2ZrO_3 (~0.7%). Its ^{27}Al MAS NMR spectrum showed three distinct resonances (Figure 2b). Since Al is a quadrupolar nuclei, the spectrum was simulated to account for the second-order quadrupolar induced shifts and values for the isotropic chemical shifts of the resonances of ~ 79 ppm, ~ 68 ppm and ~10.5 ppm were extracted (Figure S1). These values are similar to those reported in the literature[8,33,34,37,41]. Al in tetrahedral environments (AlO_4) has been reported to have shifts around 50 - 90 ppm whereas Al in octahedral environments (AlO_6) to shifts around −10 - 20 ppm[50]. Thus, the first two resonances can tentatively be ascribed to Al in a tetrahedral environment and the third resonance to Al in an octahedral environment. The signal at ~10.5 ppm is therefore ascribed to the side-product, $LaAlO_3$, which was also observed in the SXRD pattern.

Excess Li_2CO_3 is typically used for synthesis of Li containing compounds to account for Li loss at high temperatures. This can lead to the formation of Li containing side-products depending on the chemical composition of precursor used. Gamma $LiAlO_2$ (γ-$LiAlO_2$) has been observed as a side-product in XRD analysis of Al rich Al-LLZO powders in a few studies[51–53]. Hence, γ-$LiAlO_2$ was synthesised and its SXRD pattern is shown in Figure S2. Its ^{27}Al MAS NMR spectrum was collected and an excellent match between the γ-$LiAlO_2$ and the LLZO resonance with an isotropic shift of ~ 79 ppm is seen on overlapping the two spectra (Figure 2c).

To further confirm the existence of γ-$LiAlO_2$ in the sample, a ^{27}Al DQ-SQ experiment was performed. This 2D experiment excites the ^{27}Al central transitions of the I = 5/2 nucleus, connecting two different nuclei via their dipolar coupling and hence spatial proximity. A diagonal signal at a frequency 2*v* in the indirect, and *v* in the direct dimension in the 2D DQ-SQ spectrum indicates spatial proximity between nuclei (in this case Al) with identical isotropic shifts[48,54]. Consistent with this, a diagonal signal is clearly seen for the $LaAlO_3$ side-product signal (Figure 2d), where each Al is surrounded by six other Al sites at distances of approximately 3.8 Å[55]. A second signal is also seen at ~79 ppm, but not at ~68 ppm, indicating that the Al ions that give rise to the resonance at ~79 ppm are in Al-rich local environments, but those that give rise to the ~68 ppm resonance are not. This is again consistent with the assignment of the ~79 ppm resonance to γ-$LiAlO_2$, a structure where the tetrahedrally coordinated Al^{3+} ions are nearby four Al^{3+} ions in their first cation coordination shells at around 3.1 Å[56].

Upon fitting the ^{27}Al MAS NMR spectrum of Al-LLZO +10%Li (Figure S2), it was found that about 45.4% of the total Al goes into $LaAlO_3$, so rest of the Al should have been incorporated into other phases. In the extreme case, if we assume that all of the rest of the Al goes into the LLZO lattice, then about ~ 1.57 Al atoms occupy each unit cell (i.e., there is a partially occupancy of 0.065 of Al in the 24d sites, as detailed in the SI). The DQ-SQ spectrum only couples two Al-nuclei both present in the |+½> or |-½> eigenstate, reducing the probability that one detectable ^{27}Al spin is adjacent to another to 1/6. This means that the probability that one DQ-SQ observable Al-nuclei is next to another in a 24d site in LLZO is 0.043 (a 24d site only has four nearby 24d sites, which are at a distance of 3.98 Å, Table 1). Unless there is significant clustering of Al atoms in LLZO, no cross-peak are expected in the DQ-SQ spectra.

DQ-SQ spectra were also recorded as a function of evolution/refocussing times (Figure S3), the cross-peaks growing and reaching a maximum at ~ 4 rotor periods (95.2 μs) for $LaAlO_3$ and ~ 6 rotor periods (142.8 μs) for γ–$LiAlO_2$. The $LaAlO_3$ cross-peak signal intensity dropped steadily after the maxima and dropping to zero whereas intensity of the cross-peak corresponding to γ–$LiAlO_2$ decreases but is still present even after 16 rotor periods (380.8 μs). The $LaAlO_3$ cross-peak also has a higher intensity at maxima as compared to that of γ–$LiAlO_2$; this is most likely due to the larger amount of $LaAlO_3$ present in the sample. The more steady increase in the γ–$LiAlO_2$ cross peak intensity *vs.* that from $LaAlO_3$ is ascribed to the difference in numbers and distances of the Al spins in the first cation coordination shells – a Al spin in

γ–$LiAlO_2$ has four nearby Al ions with Al-Al distances of 3.12 Å, and a further two at 4.05 Å, while the Al spins in $LaAlO_3$ have six nearby Al at 3.79 Å (Table 1). The DQ/SQ relaxation rates of the two environments will also contribute to signal decay. Even after longer mixing times, cross peaks involving second coordination shells of Al cations will not be intense as second shell of 24d Al neighbours are more than 5.5 Å apart. Therefore, we assign the ~79 ppm resonance to γ-$LiAlO_2$, even though no evidence for this phase is seen in the SXRD pattern. The ~68 ppm resonance is assigned to Al in the 24d site in the LLZO lattice in agreement with previous DFT studies, which Al-substitution on this site was associated with the lowest energy[36,41].

Table 1: Number of nearest Al neighbours for an Al atom in an 24d site along with the distance (within ~ 6 Å) between them in γ–$LiAlO_2$, $LaAlO_3$ and Al-LLZO, calculated from their respective ICSD files. The number of Al neighbours and the distance between the Al neighbours along with their relaxation rates determine the intensity of the cross-peak in the DQ-SQ spectrum.

γ–$LiAlO_2$		**$LaAlO_3$**		**Al-LLZO**	
4 Al-Al	3.12 Å	6 Al-Al	3.79 Å	4 Al – Al 24d	3.98 Å
2 Al-Al	4.05 Å	6 Al-Al	5.35(62) Å	8 Al – Al 24d	6.07 Å
4 Al-Al	4.93 Å	6 Al-Al	5.36(46) Å		
4 Al-Al	5.17 Å				
4 Al-Al	5.34 Å				
4 Al-Al	5.42 Å				
2 Al-Al	5.68 Å				

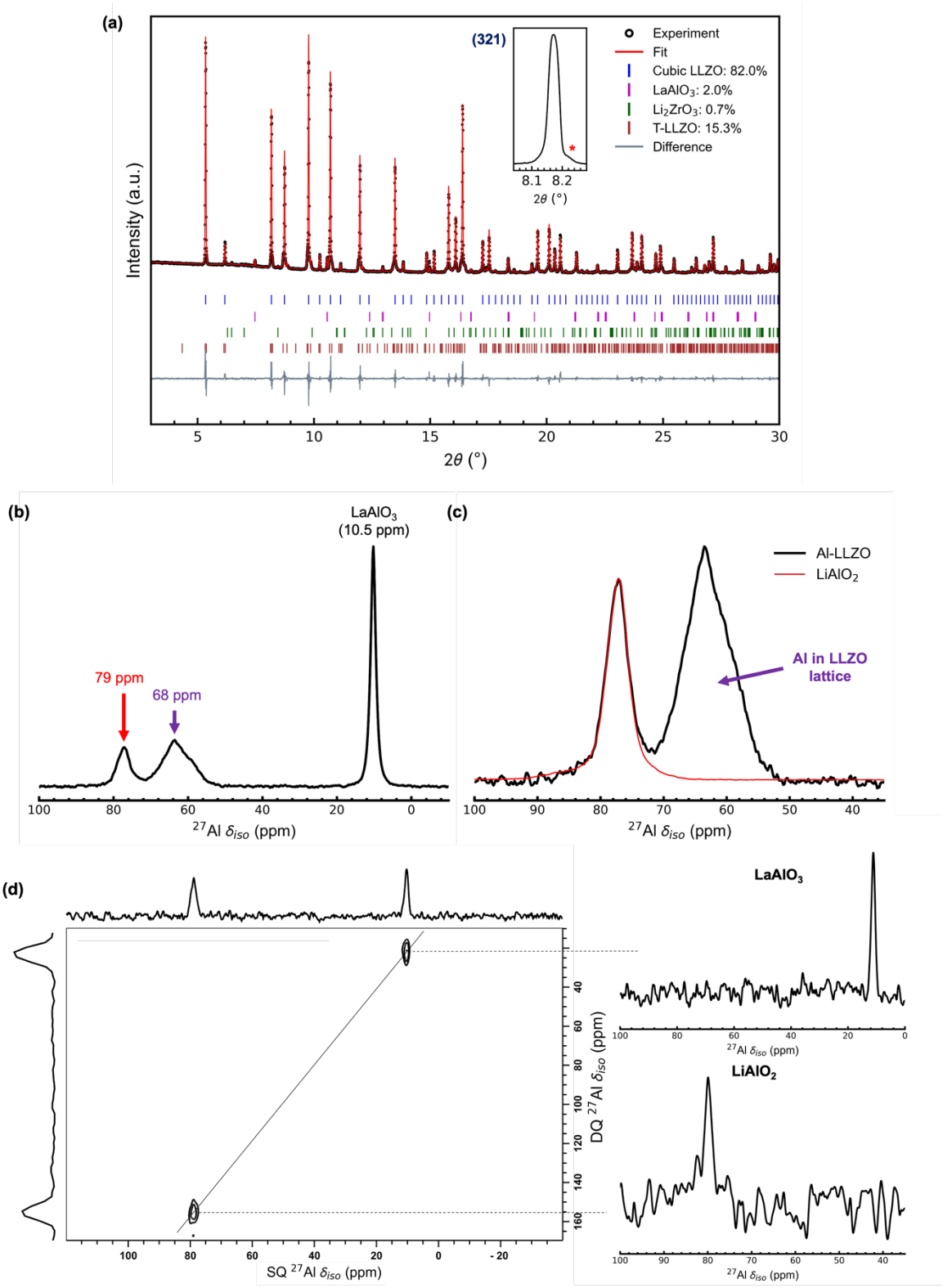

Figure 2: (a) SXRD pattern (λ = 0.493 Å) of Al-LLZO synthesised with 10% excess Li in the precursors along with its Rietveld refinement to extract phase fraction of LLZO and the side-products, the inset showing the (321) LLZO reflection (where * indicates the tetragonal LLZO phase). (b) ^{27}Al MAS NMR spectrum of the same Al-LLZO sample; the isotropic chemical shifts (in ppm) of the three resonances are marked. (c) An enlargement of the same spectrum to show the resonances corresponding to Al in tetrahedral environments (black). The LLZO ^{27}Al spectrum is overlayed with the spectrum of γ-$LiAlO_2$ (red curve), where the γ-$LiAlO_2$ spectrum was scaled

to match the intensity of the resonance at 79 ppm in the Al-LLZO spectrum. (d) DQ-SQ 2D spectrum for the same Al-LLZO with a refocussing time of 6 rotor periods; slices through the indirect (DQ) dimension are shown on the right, taken at positions indicated by the dashed lines. A $BR2_2^1$ recoupling sequence was used to probe the dipolar through space interactions between the ^{27}Al nuclei. Where appropriate, the assignments of the resonances are marked (see text).

3.2. Effect of Li excess in the precursors on the ^{27}Al MAS NMR spectrum of Al-LLZO

To further test the hypothesis that γ-$LiAlO_2$ forms during synthesis, Al-LLZO was synthesised with precursors with the exact stoichiometric of LLZO i.e., with no excess Li (Al-LLZO +0%Li), and its SXRD pattern is shown in Figure 3a.

A close inspection of the SXRD patterns of the Al-LLZO +0%Li and Al-LLZO +10%Li samples (Figures 2(a) and 3(a)) showed some tetragonal phase formation when excess Li is used, whereas no tetragonal phase was observed when excess Li was not used in the precursors. This is most likely due to sufficient incorporation of Al in LLZO lattice for cubic phase formation when excess Li is not used, strongly suggesting some excess Li can be accompanied by the formation of lithium aluminates. Approximately 3.5% $La_2Zr_2O_7$ pyrochlore was also observed in Al-LLZO +0%Li (Figure 3b). In both the cases, small amounts of $LaAlO_3$ and $Li_2Zr_2O_3$ were observed, whereas γ-$LiAlO_2$ was not observed even in these high-resolution SXRD patterns. SEM-EDS images of these samples shown in Figure S4 show significant heterogeneity in Al distribution in the Li-rich case (Al-LLZO +10%Li) compared to the Li-poor case (Al-LLZO +0%Li).

The ^{27}Al MAS spectra of Al-LLZO +10%Li and +0%Li are compared in Figure 3c. Both the ~68 ppm (Al in LLZO) and ~10.5 ppm ($LaAlO_3$) resonances were observed in the ^{27}Al MAS NMR spectrum of the two samples but the ~79 ppm resonance assigned to γ-$LiAlO_2$ was not observed in Al-LLZO +0%Li. Furthermore, the intensity of the resonance corresponding to Al in the LLZO lattice increased (Figure 2c), whereas the $LaAlO_3$ resonance decreased slightly in intensity on adding excess Li. Given that the total amount of Al is the same in both samples, the slight decrease in $LaAlO_3$ resonance intensity implies that more Al should have gone into other phases (either LLZO or γ-$LiAlO_2$) in the Al-LLZO +0%Li sample. If the ~79 ppm resonance corresponded to an LLZO environment in which two or more Al were in close proximity (i.e., an environment that would be seen in the DQ-SQ 2D experiment), this resonance would likely have increased in intensity, rather than disappearing. Since no excess

Li was used in the synthesis, all the Li was likely consumed during the formation of LLZO and there was not enough Li available to drive γ-$LiAlO_2$ formation.

The larger implication of these observations is that while some excess Li is necessary to synthesise cubic LLZO to compensate for Li loss at elevated temperatures (1000 °C in this study) any further excess Li will instead lead to unintentional tetragonal phase formation, heterogeneity in Al distribution and γ-$LiAlO_2$ in the final product. The deleterious effect of excess Li in precursors resulting in tetragonal phase formation has recently been reported in the case of Ga-LLZO[57].

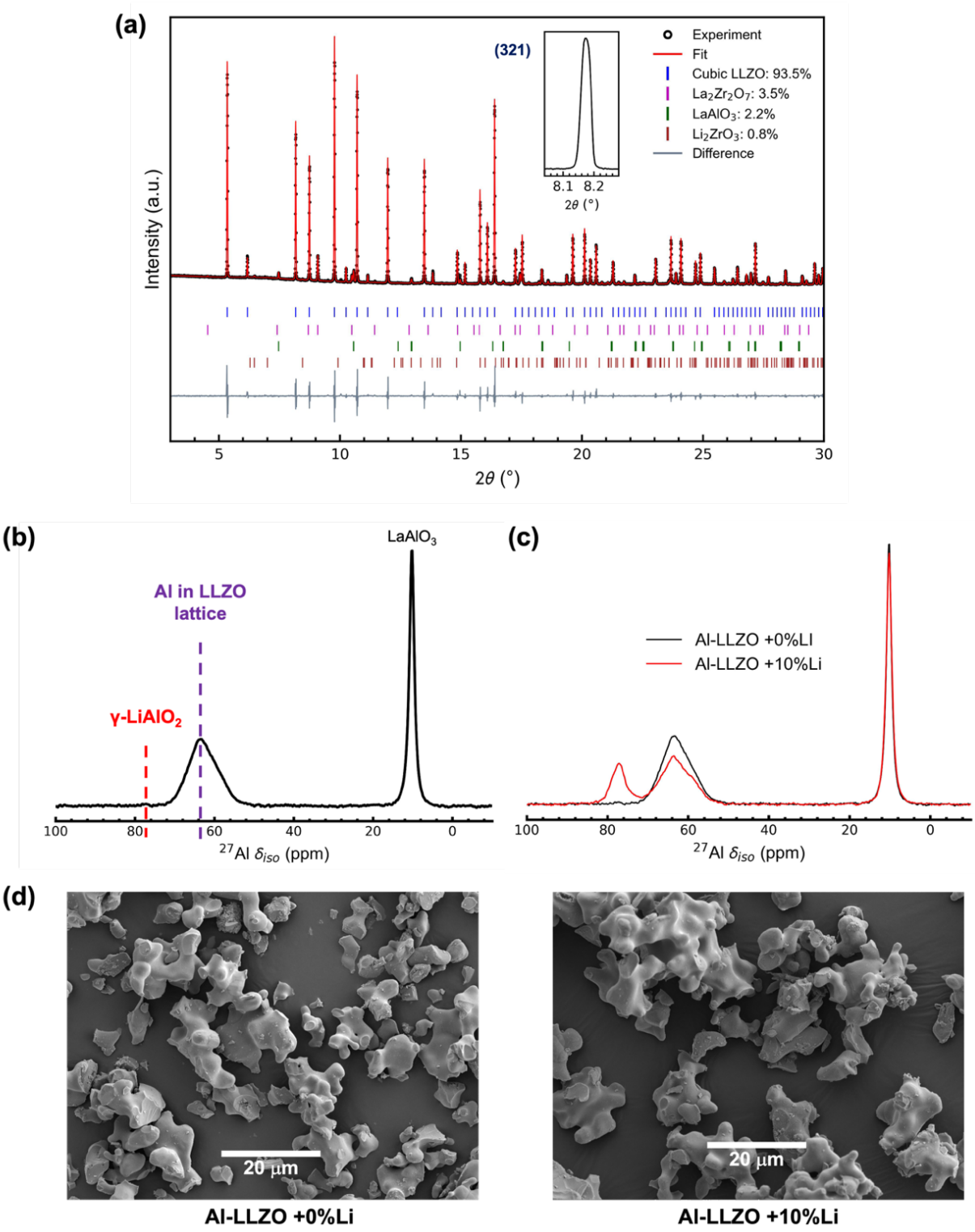

Figure 3: (a) SXRD pattern (λ = 0.493 Å) of Al-LLZO powder synthesised with no excess Li in the precursors (Al-LLZO +0%Li) with an inset showing the (321) reflection of Al-LLZO. (b) ^{27}Al MAS NMR spectrum of the Al-LLZO +0%Li samples. (c) Comparison of ^{27}Al MAS NMR spectra of the Al-LLZO +10%Li and Al-LLZO +0%Li powders. All spectra were normalised to respective sample weights during measurements. (d) Comparison of the SEM images of Al-LLZO +10%Li and Al-LLZO +0%Li powders.

3.3. Effect of sintering on MAS NMR of Al-LLZO

To check whether γ-$LiAlO_2$ still persists after sintering, the Al-LLZO powders (synthesised with 10% excess Li, Al-LLZO +10%Li) were hot-pressed into pellets, which were then polished to remove any decomposition products ($La_2Zr_2O_7$) on the surface and ground inside a glovebox. The SXRD pattern of the hot-pressed sample (Al-LLZO +10%Li HP) is shown in Figure 4a. Rietveld refinement showed that the sample was composed mainly of cubic Al-LLZO with a reduced amount of side-products ($LaAlO_3$ and $Li_2Zr_2O_3$) as compared to the Al-LLZO +10%Li sample. Moreover, the peaks corresponding to LLZO sharpened, and the tetragonal phase disappeared suggesting some redistribution of Al due to loss of Li during hot-pressing at elevated temperatures and improved crystallinity. Similar to the previous samples, the SXRD pattern did not show any sign of γ-$LiAlO_2$.The SEM images of the cross-section of the pellet showed that Al-LLZO +10%Li HP had a similar grain size as compared to the Al-LLZO +10%Li sample (Figure 4c and 3d). A SEM-EDS map comparison showed that there was still some heterogeneity in the Al distribution, which may be due to the presence of $LaAlO_3$ or γ-$LiAlO_2$ (Figure S4).

The ^{27}Al MAS NMR spectrum of the Al-LLZO +10%Li HP sample is shown in Figure 4c. Three resonances corresponding to Al in γ-$LiAlO_2$, the LLZO lattice and $LaAlO_3$ were observed as in the Al-LLZO +10%Li sample. Upon fitting the MAS NMR spectrum of Al-LLZO +10%Li HP sample, it was found that only about ~52.7% of Al used in precursors had gone into the lattice (Figure S6). On comparing the MAS NMR spectra of Al-LLZO +10%Li HP with that of the +10%Li sample (Figure 4c), the γ-$LiAlO_2$ and LLZO resonances increased in intensity whereas that from $LaAlO_3$ substantially reduced in intensity, consistent with the SXRD results. This suggests that Al from both γ-$LiAlO_2$ and $LaAlO_3$ enter the LLZO lattice during hot-pressing, helping to explain why no tetragonal phase was observed in the SXRD pattern of Al-LLZO +10%Li HP.

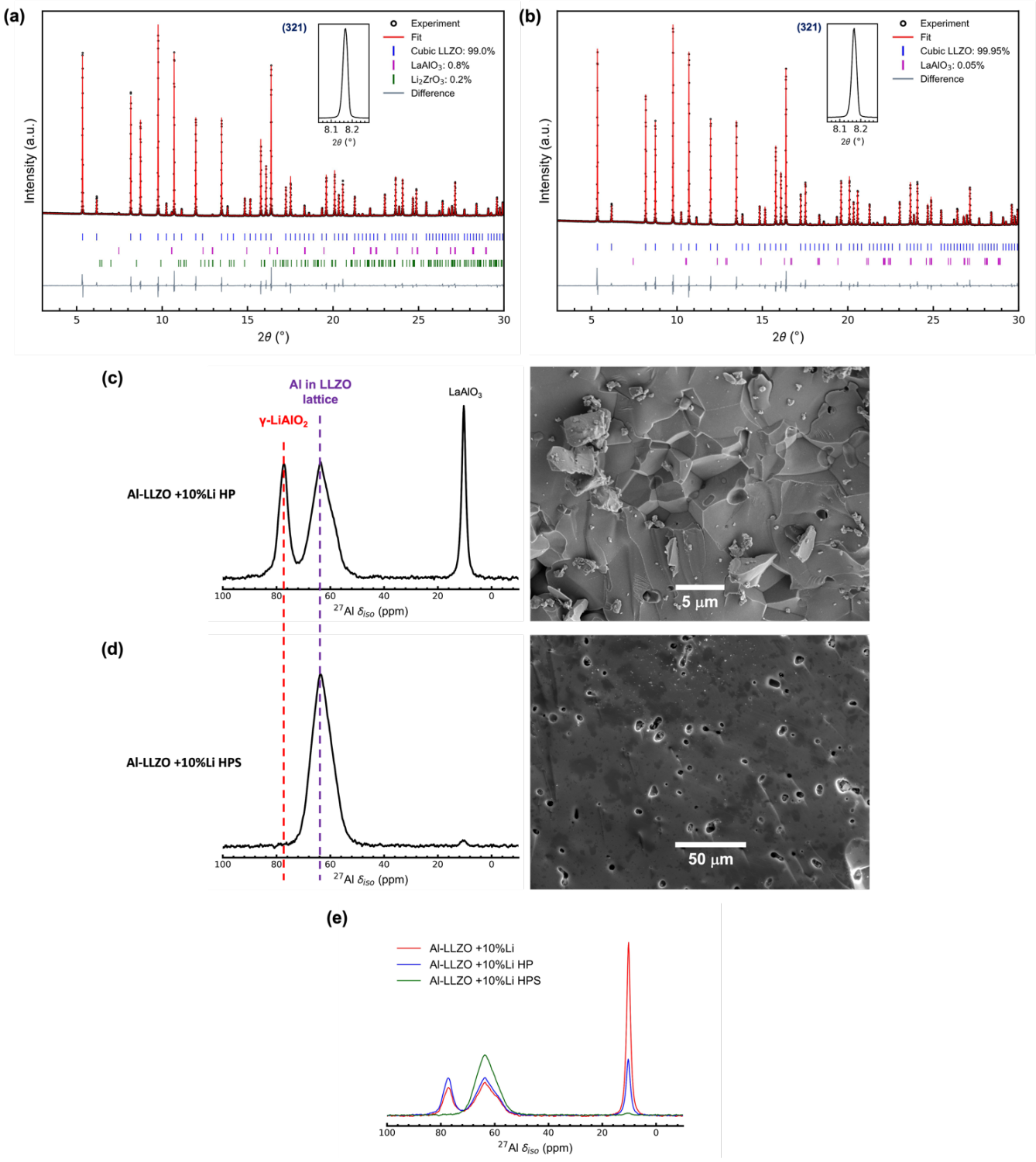

Figure 4: SXRD patterns (λ = 0.493 Å) with an inset showing the (321) LLZO reflection of (a) a hot-pressed sample of Al-LLZO +10%Li: Al-LLZO +10%Li HP and (b) hot-pressed Al-LLZO +10%Li and further sintered for 12 hrs under O_2 at 1200 °C: Al-LLZO +10%Li HP further sintered. (c) and (d) show the ^{27}Al MAS NMR spectra and corresponding SEM images of Al-LLZO +10%Li HP and Al-LLZO +10%Li HPS respectively. (e) Comparison of ^{27}Al MAS NMR spectra of the three different Al-LLZO powders.

Since γ-$LiAlO_2$ was still present in the Al-LLZO +10%Li HP sample, which had a similar grain size to the Al-LLZO +10%Li powder, the Al-LLZO +10%Li HP pellets were sintered to increase their grain size to check whether γ-$LiAlO_2$ is still present. The Al-LLZO +10%Li HP were sintered at 1200 °C for 18 hrs under flowing O_2 and the resultant pellet (Al-LLZO +10%Li HPS) was polished to remove any decomposition products ($La_2Zr_2O_7$) on the surface and was then ground inside the glovebox. Its SXRD pattern is shown in Figure 4b. Rietveld refinement showed that the sample was mainly composed of Al-LLZO and a very small amount of $LaAlO_3$; again, no γ-$LiAlO_2$ is seen. No grain boundaries were observed in the SEM image (Figure 4d) of the cross-section of the pellet suggesting large grain sizes (>200 μm). The SEM-EDS map of a pellet cross-section showed uniform distribution of Al (Figure S4).

The ^{27}Al MAS NMR spectrum of Al-LLZO +10%Li HPS (Figure 4c) shows no evidence of the γ-$LiAlO_2$ signal and only a very small $LaAlO_3$ signal was observed, consistent with the SXRD pattern. In addition, the intensity of the signal corresponding to Al in the LLZO lattice increased (Figure 4c) compared to Al-LLZO +10%Li HP sample. Upon fitting the MAS NMR spectrum, it was found that almost all of the Al (~99.1%) used in the precursors has gone into the lattice (Figure S7).

To confirm whether γ-$LiAlO_2$ signal indeed disappears in any sample with large grain sizes, a sample was prepared using an alternate route by sintering nano-sized Al-LLZO powder at 1200 °C for 12 hrs, which again resulted in large grains (~200 μm) (See Supplementary information for more details and Figure S8). The γ-$LiAlO_2$ signal was again not observed.

The disappearance of the γ-$LiAlO_2$ signal in samples with large grain sizes such as in Al-LLZO +10%Li HPS sample and its presence in small-grained samples (Al-LLZO +10%Li and Al-LLZO +10%Li HP) can be explained if γ-$LiAlO_2$ is present as a heterogeneous coating on the surface of grains or at the grain boundaries in the Al-LLZO +10%Li sample. As the sample grain size did not change drastically after hot-press sintering (Figure 3a and 4a), negligible changes are expected in the existing grain boundaries that contain γ-$LiAlO_2$ and the new grain boundaries generated from the once free surface of grains in Al-LLZO +10%Li powder will also contain γ-$LiAlO_2$ (Figure 5). Thus, the ^{27}Al MAS NMR spectrum is expected to be similar for Al-LLZO +10%Li and Al-LLZO +10%Li HP samples, as seen experimentally. When Al-LLZO 10% HP was further sintered to form pellets with large grain sizes (Al-LLZO +10%Li HPS), any thin or amorphous layer of γ-$LiAlO_2$ on the surface or in grain-boundaries of Al-LLZO +10%Li would have been absorbed into the bulk of grains during sintering. The resulting

samples have fewer grain boundaries and have too little Al in γ-$LiAlO_2$ to contribute to the ^{27}Al MAS NMR spectrum, so the signal corresponding to γ-$LiAlO_2$ disappears in these samples (Figure 5).

The location of γ-$LiAlO_2$, whether it is present in grain boundaries or at the surfaces of grains in Al-LLZO +10%Li sample will need to be examined in greater detail in a further study.

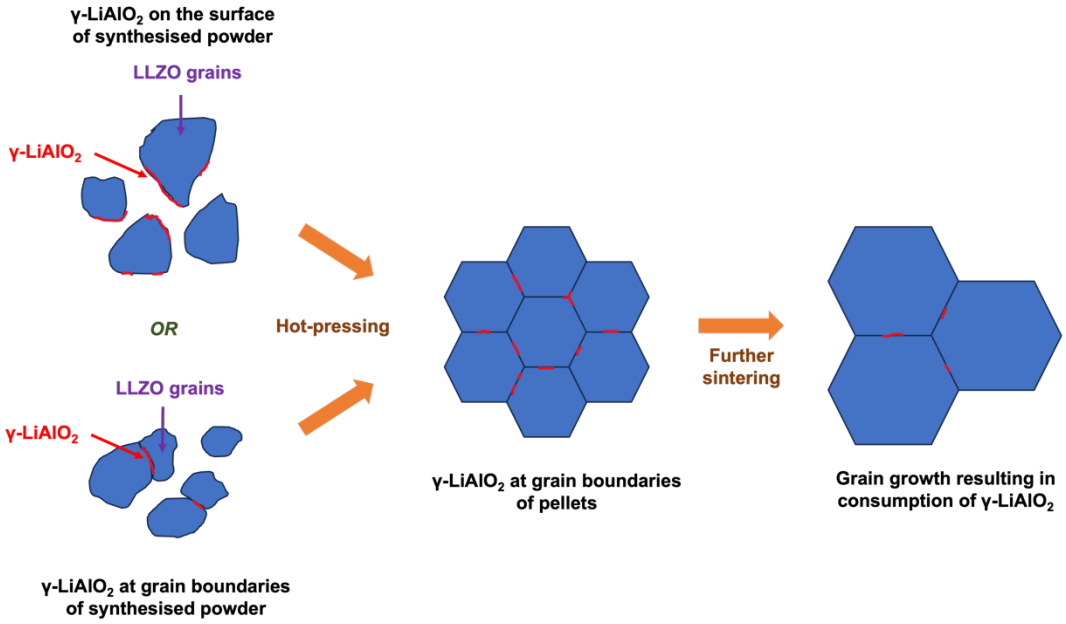

Figure 5: Representation of possible locations of γ-$LiAlO_2$ (red) in LLZO grains (blue) and the possible reasons for its disappearance in samples with larger LLZO grain sizes

3.4. Effect of γ-$LiAlO_2$ on the ionic conductivity of the sintered samples

To understand how the presence of γ-$LiAlO_2$ affects the ionic conductivity of sintered samples, blocking electrode impedance measurements were done on the two sintered samples, Al-LLZO +10%Li HP, and Al-LLZO +10%Li HPS (Figure 6a-b). The impedance plots show that the resistance of the Al-LLZO +10%Li HPS sample is not simply the sum of bulk and grain boundary resistance of Al-LLZO +10%Li HP sample (Figure 6c). Instead, the total resistance of the Al-LLZO +10%Li HP further sintered samples increases by about a factor of ~6. The Al-LLZO +10%Li HP sample showed two features corresponding to bulk and grain boundary resistance. On fitting, the samples showed a bulk conductivity of ~0.63 $mScm^{-1}$ (and a total conductivity of ~0.47 $mScm^{-1}$). By contrast the Al-LLZO +10%Li HPS sample showed only one feature corresponding to the bulk resistance and upon fitting the spectra, a bulk conductivity of 0.11 $mScm^{-1}$ was obtained.

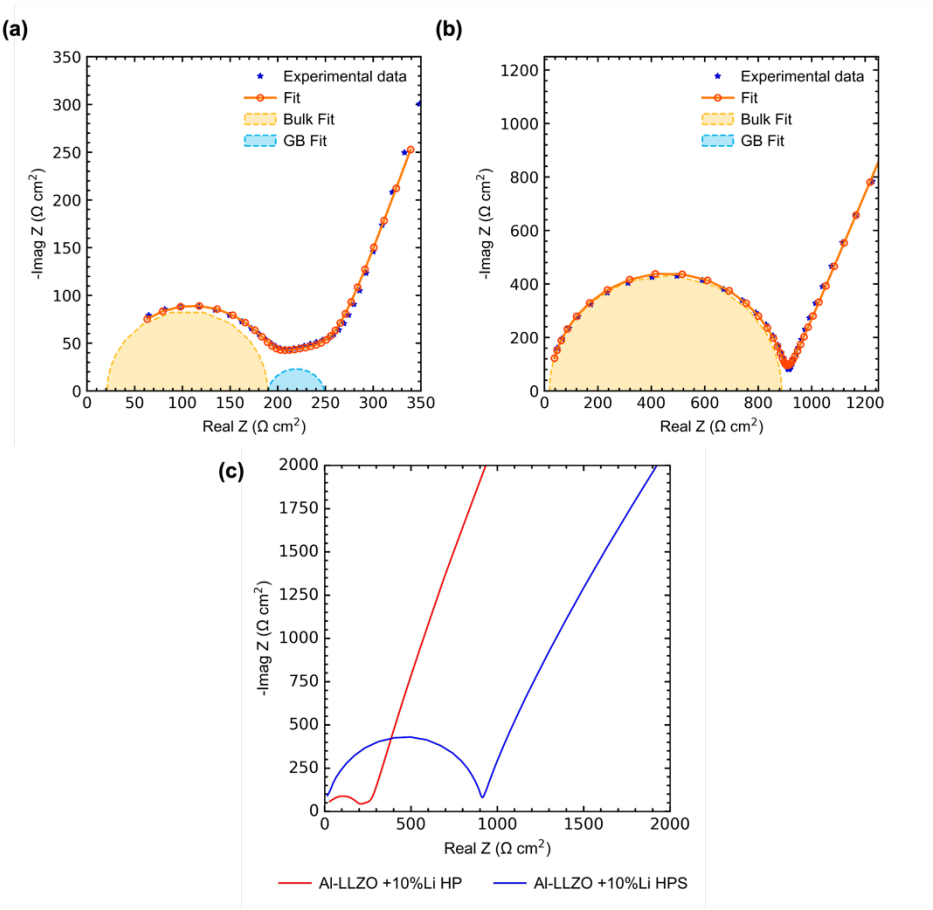

Figure 6: Blocking electrode impedance measurements of Al-LLZO (a) hot-pressed Al-LLZO powder +10%Li powder, Al-LLZO 10%Li HP and (b) hot-pressed and further sintered powder from +10%Li powder, Al-LLZO +10%Li HPS. The fit is shown along with the impedance plots. (c) Comparison of samples shown in (a) and (b)

By using the intensities of the ^{27}Al signals of the LLZO peaks in the MAS NMR spectra, the Al content in the LLZO samples can be calculated (as detailed in the SI) as approximately $Al_{0.2}Li_{6.4}La_3Zr_2O_{12}$ for Al-LLZO +10%Li HP sample and $Al_{0.36}Li_{5.92}La_3Zr_2O_{12}$ for the Al-LLZO +10%Li HPS sample. The increase in Al (and by extension decrease in Li) content in LLZO correlates with the decrease in ionic conductivity. For thermally activated ionic conduction with uncorrelated hopping, the ionic conductivity, σ can be simplified as[58]:

$$\sigma = q\, n\, u$$

where, q is charge, n is the charge carrier concentration, and u is the mobility that captures the ability of an ion (charge carriers) to move through the solid lattice. The drop in the conductivity of the Al-LLZO +10%Li HPS sample is most likely due to the reduction in charge carrier concentration (Li) due to an increase in Al concentration as compared to the Al-LLZO +10%Li HP sample. A reduction in bulk ionic conductivity with increasing Al content in the precursors has also recently been reported[59].

The existence of Al in γ-$LiAlO_2$ and the uneven distribution of Al between γ-$LiAlO_2$ and the LLZO lattice depending on synthesis conditions and grain sizes might be one of the major reasons for the wide-ranging total ionic conductivity values reported in the literature. The absence of tetragonal Al-LLZO in the Al-LLZO +10%Li HP sample suggests that ~0.19 Al per 7 Li atoms (quantified from MAS NMR spectra see supplementary information) is enough Al to form cubic LLZO, and the highest conductivity is found at the transition point between tetragonal and cubic LLZO.

3.5. ^{71}Ga MAS NMR and EIS Analysis of Ga-LLZO

Similar issues exist concerning the lattice site occupied by Ga dopant in Ga-LLZO. Ga-LLZO ($Ga_{0.2}Li_{6.3}La_3Zr_2O_{12}$) was synthesised with 5% Li excess (Ga-LLZO +5%Li) in the precursors and its SXRD pattern is shown in Figure 7a. Since excess Li in the precursors resulted in γ-$LiAlO_2$ side-product in Al-LLZO, only 5% excess Li was used in the synthesis of Ga-LLZO. Rietveld refinement showed that the sample contained ~30% tetragonal phase alongside the cubic phase and no other side-product could be identified. The SEM-EDS mapping of the synthesised powder showed regions which were rich in Ga and deficient in La and Zr (Figure S12).

^{71}Ga MAS NMR spectrum of the synthesised sample showed two distinct resonances (Figure 7a) as has been previously observed in the literature[37,41,45]. Since, ^{71}Ga is an (I = 3/2) quadrupolar nuclei, the spectrum was fitted and the isotropic chemical shifts, ~199 ppm and ~242 ppm were extracted. ^{71}Ga in tetrahedral environments (GaO_4) has been reported to have shifts around 150-250 ppm[60]. Therefore, the two resonances observed can be attributed to Ga in two distinct tetrahedral environments. $LiGaO_2$ was synthesised (SXRD pattern in Figure S9) and its ^{71}Ga MAS NMR spectrum was collected and again overlayed with that of Ga-LLZO (Figure 7a). As in the case of Al-LLZO, the match between $LiGaO_2$ and the ~242 ppm resonance observed in Ga-LLZO was very good with similar quadrupolar coupling constants (3.84 ± 0.10 MHz and 3.82 ± 0.10 MHz for $LiGaO_2$ and Ga-LLZO respectively) and asymmetry parameters (0.41 ± 0.02 and 0.40 ± 0.02 for $LiGaO_2$ and Ga-LLZO respectively) being found for the two materials. The existence of $LiGaO_2$ in the LLZO samples can explain the La and Zr deficient and Ga rich regions seen by SEM-EDS. The remaining ~199 ppm resonance can be attributed to Ga in the 24d site in the LLZO lattice.

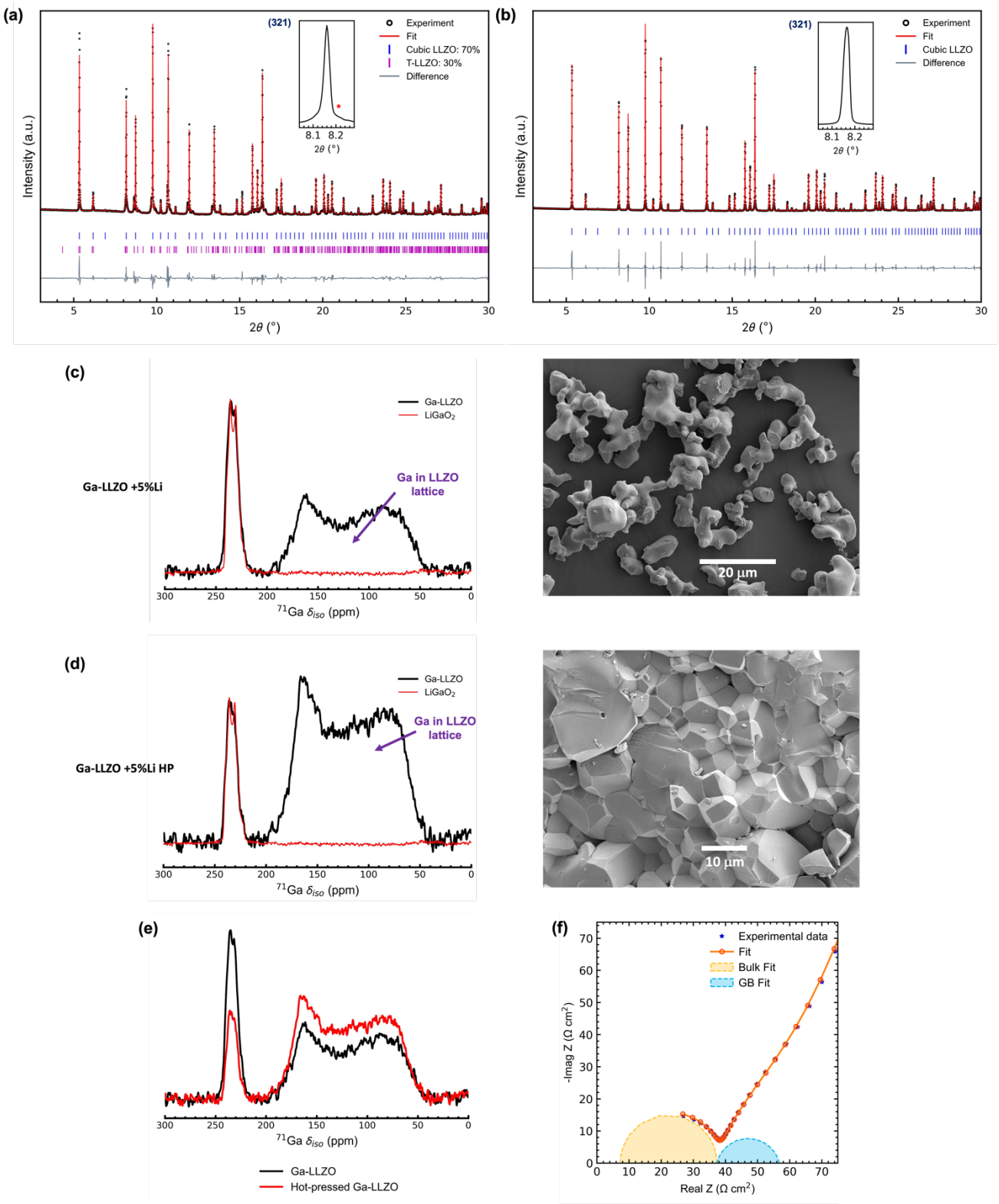

Figure 7: (a) SXRD patterns (λ = 0.493 Å) of (a) Ga-LLZO +5%Li and (b) hot-pressed sample of Ga-LLZO +5%Li (Ga-LLZO +5%Li HP) with an inset showing the peak corresponding to (321) reflection where * indicates tetragonal LLZO phase. The ^{71}Ga MAS NMR spectra of (c) Ga-LLZO +5%Li and (d) Ga-LLZO +5%Li HP (overlayed with the ^{71}Ga MAS NMR spectrum of $LiGaO_2$) and their corresponding SEM images. (e) Comparison of ^{71}Ga MAS NMR spectra of both samples. Both spectra were normalised to respective sample weights during measurements. (f) Blocking electrode impedance measurement of the Ga-LLZO +5%Li HP sample.

To check whether $LiGaO_2$ persisted after sintering, the synthesised Ga-LLZO +5%Li powder was hot pressed (Ga-LLZO +5%Li HP) and its SXRD pattern is shown in Figure 7b. Rietveld refinement showed that the sample was composed entirely of cubic phase LLZO. The SEM images of the cross-section of the Ga-LLZO +5%Li HP pellet showed that it had grains of similar size as in the Ga-LLZO +5%Li sample (Figure 7a-b) and the EDS map showed similar La and Zr deficient and Ga rich regions as in the Ga-LLZO +5%Li sample. The ^{71}Ga MAS NMR spectrum of the Ga-LLZO +5%Li HP sample showed two resonances with identical isotropic chemical shifts as those in the Ga-LLZO +5%Li sample i.e., ~199 ppm (Ga in LLZO lattice) and ~242 ppm ($LiGaO_2$). These observations are consistent with the recent observation of $LiGaO_2$ in sintered Ga-LLZO pellets by high resolution transmission electron microscopy[61]. The present work suggests that $LiGaO_2$ is present not just in sintered pellets but also in the synthesised powders of Ga-LLZO.

A comparison of the two ^{71}Ga MAS NMR spectra (Figure 7c) showed that upon hot-pressing the intensity of the ~242 ppm ($LiGaO_2$) resonance was reduced while the intensity of the ~199 ppm resonance (Ga in LLZO lattice) increased indicating that some Ga incorporates into the LLZO lattice from $LiGaO_2$ leading to complete cubic phase formation (as seen by SXRD).

The ionic conductivity of the hot-pressed pellets was measured by EIS. In the blocking electrode impedance plot (Figure 7d), the hot-pressed samples showed two features corresponding to bulk and grain boundary resistance. On fitting, a bulk ionic conductivity of 2.8 $mScm^{-1}$ and a total ionic conductivity of 1.75 $mScm^{-1}$ was obtained which is among the highest reported total and bulk ionic conductivities for Ga-LLZO[20,44]. A similar dependence of Li-ion conductivity on the Ga content in the LLZO lattice can be expected as in the case of Al-LLZO.

3.6 ^{27}Al and ^{71}Ga MAS NMR of $LiAl_{0.5}Ga_{0.5}O_2$

It has been reported in the literature that upon simultaneous doping of LLZO with Al and Ga, the resonance with higher chemical shift moves to higher frequencies in the ^{27}Al MAS NMR spectrum while the resonance with higher chemical shift broadens in ^{71}Ga MAS NMR spectrum[37,41]. Since co-doping in LLZO may also result in substitution of Al into $LiGaO_2$ and vice-versa, $LiAl_{0.5}Ga_{0.5}O_2$ was prepared by mixing the precursors needed for $LiAlO_2$ and $LiGaO_2$ in a 1:1 ratio and heating at conditions similar to those used to prepare LLZO. The SXRD pattern of the resultant sample is two-phase comprising of both γ–$LiAlO_2$ and $LiGaO_2$, but with shifted peak positions suggesting that some Al was incorporated into $LiGaO_2$ and vice-

versa (Figure S13). The ^{27}Al MAS NMR spectrum showed shifting and broadening of the resonance towards higher frequencies compared to the undoped case (Figure 8) whereas the ^{71}Ga MAS NMR spectrum showed broadening of the resonance (along with a small shift). This further confirms that the resonance with higher chemical shift in both ^{27}Al and ^{71}Ga MAS NMR spectra of LLZO co-doped with Al and Ga is due to the side products, γ–$LiAlO_2$ or $LiGaO_2$ with Ga and Al incorporation respectively.

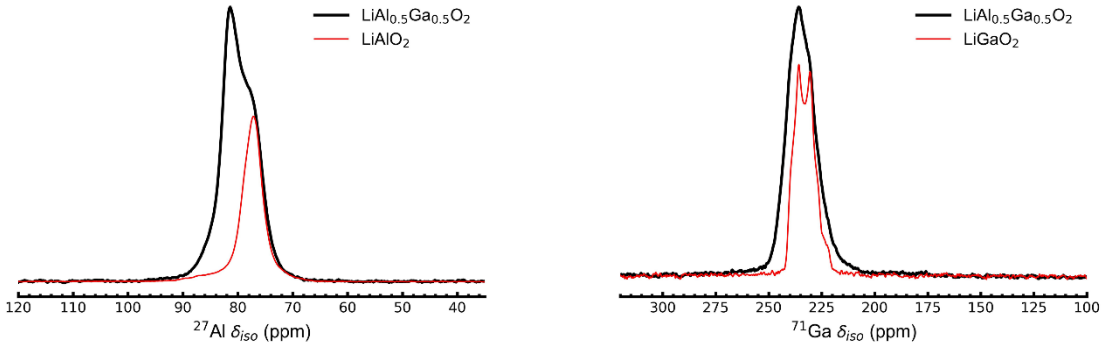

Figure 8: ^{27}Al (left) and ^{71}Ga (right) MAS NMR spectra comparison of γ–$LiAlO_2$ and $LiGaO_2$ with $LiAl_{0.5}Ga_{0.5}O_2$..

A recent report suggested that Li configuration in the first cation coordination shell around the dopant can influence the dopants' isotropic chemical shift[41], the more symmetric environment surrounded by 4 Li ions giving rise to higher shifts and much smaller quadrupolar environments. On this basis, the ~ 79 ppm and ~ 242 ppm resonances in the ^{27}Al and ^{71}Ga MAS NMR spectra respectively were assigned to these configurations. The ~ 79 ppm resonance was not seen in the sample prepared in this work with no excess Li (Al-LLZO +0%Li) which has more Al (and hence less Li), but it was seen in the sample prepared with 10% excess Li (Al-LLZO +10%Li) which had less Al (and hence more Li).

More Al atoms with 4 Li around them should have been more pronounced in the Al-LLZO +0%Li sample as there was more Al in the lattice than in the Al-LLZO +10%Li sample. However, this study did not account for the effect of Li mobility on the spectra. At RT, due to the Li motion around the dopant[31,62], the effect of Li configuration around dopants is not observed. However, at very low temperatures, where the Li motion can be hindered, the ordering of Li around the dopant might influence the isotropic chemical shift of dopants, and additional broadening of the LLZO resonances might be expected.

4. Conclusion

In this work, we have shown that Al and Ga dopants occupy only the 24d site in LLZO lattice putting rest to the speculation regarding dopant site occupancy in the battery community. The additional higher frequency resonance observed in this work and in previous studies in both ^{27}Al and ^{71}Ga MAS NMR spectra of Al- and Ga-LLZO has been identified as being due to the side-products, γ-$LiAlO_2$/$LiGaO_2$. These side products have been found to exist even in hot-pressed Al-LLZO and Ga-LLZO samples. Since γ-$LiAlO_2$ and $LiGaO_2$ are not observed in the SXRD patterns of LLZO samples, their presence has likely been overlooked by the community (including us).

The distribution of dopants between these side-products and the LLZO lattice has been found to considerably affect the ionic conductivity of LLZO. A decrease in ionic conductivity with increase in dopant concentration in LLZO lattice was observed, which is ascribed to the reduction in charge carrier concentration as the amount of dopant increases. Thus, to achieve high ionic conductivity in LLZO, it is necessary to identify the minimum dopant concentration (and hence maximum Li content) required for the tetragonal to cubic phase transition through careful synthesis of LLZO. Finally, it is emphasised that some excess Li is needed to synthesise pure cubic phase LLZO at high temperatures (1000 °C) to account for Li loss, but any further excess Li will lead to the formation Al or Ga-containing side-products, resulting in the formation of the poorly ionically conducting tetragonal phase LLZO formation. The results from this study further suggest that the structure of solid-state electrolytes and Li/transition metal mixing in other Li containing compounds such as NMC cathodes need to be carefully studied as a function of Li-excess content in the precursors.

Supporting information

SXRD of samples, Fitting data of MAS NMR spectra, SEM-EDS maps, Experimental methods. This material is available free of charge via the Internet at http://pubs.acs.org

Acknowledgement

S.V. acknowledges funding from the Cambridge Commonwealth European and International Trust, Faraday Institution (SOLBAT, FIRG007) and Royal Society (RP/R1/180147). A.H.B acknowledges funding from Advanced EU ERC grant (EC H2020 835073). S.N. thanks the Royal Society (United Kingdom) and Science and Engineering Research Board (Government of India) for the award of Newton-Bhabha International Fellowship (NIF/R1/180075). C.P.G

thanks the EU via an Advanced EU ERC grant (EC H2020 835073). Professor Norman Fleck and Professor Vikram Deshpande from Department of Engineering, University of Cambridge are thanked for letting us use their labs for sample preparation. We acknowledge Dr Steffen P. Emge for his help during early stages of this work. We thank Diamond Light Source, Oxford, United Kingdom for access to beamline I11 for synchrotron XRD measurements under rapid access (CY34151) and under BAG proposal (CY28349). The UK High-Field Solid-State NMR Facility used in this research was funded by EPSRC and BBSRC (EP/T015063/1) as well as, for the 1 GHz instrument, EP/R029946/1.

References

(1) Zhu, Y.; He, X.; Mo, Y. Origin of Outstanding Stability in the Lithium Solid Electrolyte Materials: Insights from Thermodynamic Analyses Based on First-Principles Calculations. *ACS Appl Mater Interfaces* **2015**, *7* (42), 23685–23693. https://doi.org/10.1021/acsami.5b07517.

(2) Zhang, Z.; Shao, Y.; Lotsch, B.; Hu, Y.-S.; Li, H.; Janek, J.; Nazar, L. F.; Nan, C.-W.; Maier, J.; Armand, M.; Chen, L. New Horizons for Inorganic Solid State Ion Conductors. *Energy Environ Sci* **2018**, *11* (8), 1945–1976. https://doi.org/10.1039/C8EE01053F.

(3) Wang, C.; Fu, K.; Kammampata, S. P.; McOwen, D. W.; Samson, A. J.; Zhang, L.; Hitz, G. T.; Nolan, A. M.; Wachsman, E. D.; Mo, Y.; Thangadurai, V.; Hu, L. Garnet-Type Solid-State Electrolytes: Materials, Interfaces, and Batteries. *Chem Rev* **2020**, *120* (10), 4257–4300. https://doi.org/10.1021/acs.chemrev.9b00427.

(4) Murugan, R.; Thangadurai, V.; Weppner, W. Fast Lithium Ion Conduction in Garnet-Type Li7La 3Zr2O12. *Angewandte Chemie - International Edition* **2007**, *46* (41), 7778–7781. https://doi.org/10.1002/anie.200701144.

(5) Awaka, J.; Kijima, N.; Hayakawa, H.; Akimoto, J. Synthesis and Structure Analysis of Tetragonal Li7La3Zr2O12 with the Garnet-Related Type Structure. *J Solid State Chem* **2009**, *182* (8), 2046–2052. https://doi.org/10.1016/j.jssc.2009.05.020.

(6) Awaka, J.; Takashima, A.; Kataoka, K.; Kijima, N.; Idemoto, Y.; Akimoto, J. Crystal Structure of Fast Lithium-Ion-Conducting Cubic Li 7La3Zr2O12. *Chem Lett* **2011**, *40* (1), 60–62. https://doi.org/10.1246/cl.2011.60.

(7) Percival, J.; Kendrick, E.; Smith, R. I.; Slater, P. R. Cation Ordering in Li Containing Garnets: Synthesis and Structural Characterisation of the Tetragonal System, Li7La3Sn2O12. *Dalton Transactions* **2009**, No. 26, 5177. https://doi.org/10.1039/b907331k.

(8) Geiger, C. A.; Alekseev, E.; Lazic, B.; Fisch, M.; Armbruster, T.; Langner, R.; Fechtelkord, M.; Kim, N.; Pettke, T.; Weppner, W. Crystal Chemistry and Stability of "Li7La 3Zr2O12" Garnet: A Fast Lithium-Ion Conductor. *Inorg Chem* **2011**, *50* (3), 1089–1097. https://doi.org/10.1021/ic101914e.

(9) Kotobuki, M.; Kanamura, K.; Sato, Y.; Yoshida, T. Fabrication of All-Solid-State Lithium Battery with Lithium Metal Anode Using Al2O3-Added Li7La3Zr 2O12 Solid Electrolyte. *J Power Sources* **2011**, *196* (18), 7750–7754. https://doi.org/10.1016/j.jpowsour.2011.04.047.

(10) Rangasamy, E.; Wolfenstine, J.; Sakamoto, J. The Role of Al and Li Concentration on the Formation of Cubic Garnet Solid Electrolyte of Nominal Composition Li 7La 3Zr 2O 12. *Solid State Ion* **2012**, *206*, 28–32. https://doi.org/10.1016/j.ssi.2011.10.022.

(11) Buschmann, H.; Berendts, S.; Mogwitz, B.; Janek, J. Lithium Metal Electrode Kinetics and Ionic Conductivity of the Solid Lithium Ion Conductors "Li 7La 3Zr 2O 12" and

Li 7-XLa 3Zr 2-XTa XO 12 with Garnet-Type Structure. *J Power Sources* **2012**, *206*, 236–244. https://doi.org/10.1016/j.jpowsour.2012.01.094.

(12) Rangasamy, E.; Wolfenstine, J.; Allen, J.; Sakamoto, J. The Effect of 24c-Site (A) Cation Substitution on the Tetragonal-Cubic Phase Transition in Li7-XLa3-XAxZr 2O12 Garnet-Based Ceramic Electrolyte. *J Power Sources* **2013**, *230*, 261–266. https://doi.org/10.1016/j.jpowsour.2012.12.076.

(13) Wolfenstine, J.; Ratchford, J.; Rangasamy, E.; Sakamoto, J.; Allen, J. L. Synthesis and High Li-Ion Conductivity of Ga-Stabilized Cubic Li 7La 3Zr 2O 12. *Mater Chem Phys* **2012**, *134* (2–3), 571–575. https://doi.org/10.1016/j.matchemphys.2012.03.054.

(14) El Shinawi, H.; Janek, J. Stabilization of Cubic Lithium-Stuffed Garnets of the Type "Li 7La3Zr2O12" by Addition of Gallium. *J Power Sources* **2013**, *225*, 13–19. https://doi.org/10.1016/j.jpowsour.2012.09.111.

(15) Allen, J. L.; Wolfenstine, J.; Rangasamy, E.; Sakamoto, J. Effect of Substitution (Ta, Al, Ga) on the Conductivity of Li 7La 3Zr 2O 12. *J Power Sources* **2012**, *206*, 315–319. https://doi.org/10.1016/j.jpowsour.2012.01.131.

(16) Wagner, R.; Redhammer, G. J.; Rettenwander, D.; Tippelt, G.; Welzl, A.; Taibl, S.; Fleig, J.; Franz, A.; Lottermoser, W.; Amthauer, G. Fast Li-Ion-Conducting Garnet-Related Li7-3xFexLa3Zr2O12 with Uncommon I4-3d Structure. *Chemistry of Materials* **2016**, *28* (16), 5943–5951. https://doi.org/10.1021/acs.chemmater.6b02516.

(17) Ramzy, A.; Thangadurai, V. Tailor-Made Development of Fast Li Ion Conducting Garnet-like Solid Electrolytes. *ACS Appl Mater Interfaces* **2010**, *2* (2), 385–390. https://doi.org/10.1021/am900643t.

(18) Dhivya, L.; Janani, N.; Palanivel, B.; Murugan, R. Li^{+} Transport Properties of W Substituted $Li_7La_3Zr_2O_{12}$ Cubic Lithium Garnets. *AIP Adv* **2013**, *3* (8), 082115. https://doi.org/10.1063/1.4818971.

(19) Rettenwander, D.; Redhammer, G.; Preishuber-Pflügl, F.; Cheng, L.; Miara, L.; Wagner, R.; Welzl, A.; Suard, E.; Doeff, M. M.; Wilkening, M.; Fleig, J.; Amthauer, G. Structural and Electrochemical Consequences of Al and Ga Cosubstitution in Li7La3Zr2O12 Solid Electrolytes. *Chemistry of Materials* **2016**, *28* (7), 2384–2392. https://doi.org/10.1021/acs.chemmater.6b00579.

(20) Wu, J.-F.; Chen, E.-Y.; Yu, Y.; Liu, L.; Wu, Y.; Pang, W. K.; Peterson, V. K.; Guo, X. Gallium-Doped $Li_7La_3Zr_2O_{12}$ Garnet-Type Electrolytes with High Lithium-Ion Conductivity. *ACS Appl Mater Interfaces* **2017**, *9* (2), 1542–1552. https://doi.org/10.1021/acsami.6b13902.

(21) Robben, L.; Merzlyakova, E.; Heitjans, P.; Gesing, T. M. Symmetry Reduction Due to Gallium Substitution in the Garnet Li6.43(2)Ga0.52(3)La2.67(4)Zr2O12. *Acta Crystallogr E Crystallogr Commun* **2016**, *72*, 287–289. https://doi.org/10.1107/S2056989016001924.

(22) Rettenwander, D.; Wagner, R.; Langer, J.; Maier, M. E.; Wilkening, M.; Amthauer, G. Crystal Chemistry of "Li7 La3 Zr2 O12" Garnet Doped with Al, Ga, and Fe: A Short Review on Local Structures as Revealed by NMR and Mößbauer Spectroscopy

Studies. *European Journal of Mineralogy* **2016**, *28* (3), 619–629. https://doi.org/10.1127/ejm/2016/0028-2543.

(23) Han, J.; Zhu, J.; Li, Y.; Yu, X.; Wang, S.; Wu, G.; Xie, H.; Vogel, S. C.; Izumi, F.; Momma, K.; Kawamura, Y.; Huang, Y.; Goodenough, J. B.; Zhao, Y. Experimental Visualization of Lithium Conduction Pathways in Garnet-Type Li7La3Zr2O12. *Chemical Communications* **2012**, *48* (79), 9840–9842. https://doi.org/10.1039/c2cc35089k.

(24) Bernstein, N.; Johannes, M. D.; Hoang, K. Origin of the Structural Phase Transition in Li7La3Zr2O12. *Phys Rev Lett* **2012**, *109* (20), 205702. https://doi.org/10.1103/PhysRevLett.109.205702.

(25) Kuhn, A.; Epp, V.; Schmidt, G.; Narayanan, S.; Thangadurai, V.; Wilkening, M. Spin-Alignment Echo NMR: Probing Li $^{+}$ Hopping Motion in the Solid Electrolyte Li $_{7}$ La $_{3}$ Zr $_{2}$ O $_{12}$ with Garnet-Type Tetragonal Structure. *Journal of Physics: Condensed Matter* **2012**, *24* (3), 035901. https://doi.org/10.1088/0953-8984/24/3/035901.

(26) Jalem, R.; Yamamoto, Y.; Shiiba, H.; Nakayama, M.; Munakata, H.; Kasuga, T.; Kanamura, K. Concerted Migration Mechanism in the Li Ion Dynamics of Garnet-Type Li 7La3Zr2O12. *Chemistry of Materials* **2013**, *25* (3), 425–430. https://doi.org/10.1021/cm303542x.

(27) Meier, K.; Laino, T.; Curioni, A. Solid-State Electrolytes: Revealing the Mechanisms of Li-Ion Conduction in Tetragonal and Cubic LLZO by First-Principles Calculations. *Journal of Physical Chemistry C* **2014**, *118* (13), 6668–6679. https://doi.org/10.1021/jp5002463.

(28) Klenk, M.; Lai, W. Local Structure and Dynamics of Lithium Garnet Ionic Conductors: Tetragonal and Cubic Li7La3Zr2O7. *Physical Chemistry Chemical Physics* **2015**, *17* (14), 8758–8768. https://doi.org/10.1039/c4cp05690f.

(29) García Daza, F. A.; Bonilla, M. R.; Llordés, A.; Carrasco, J.; Akhmatskaya, E. Atomistic Insight into Ion Transport and Conductivity in Ga/Al-Substituted Li 7 La 3 Zr 2 O 12 Solid Electrolytes. *ACS Appl Mater Interfaces* **2019**, *11* (1), 753–765. https://doi.org/10.1021/acsami.8b17217.

(30) Bonilla, M. R.; García Daza, F. A.; Carrasco, J.; Akhmatskaya, E. Exploring Li-Ion Conductivity in Cubic, Tetragonal and Mixed-Phase Al-Substituted Li7La3Zr2O12 Using Atomistic Simulations and Effective Medium Theory. *Acta Mater* **2019**, *175*, 426–435. https://doi.org/10.1016/j.actamat.2019.06.033.

(31) Posch, P.; Lunghammer, S.; Berendts, S.; Ganschow, S.; Redhammer, G. J.; Wilkening, A.; Lerch, M.; Gadermaier, B.; Rettenwander, D.; Wilkening, H. M. R. Ion Dynamics in Al-Stabilized Li7La3Zr2O12 Single Crystals – Macroscopic Transport and the Elementary Steps of Ion Hopping. *Energy Storage Mater* **2020**, *24*, 220–228. https://doi.org/10.1016/j.ensm.2019.08.017.

(32) Momma, K.; Izumi, F. VESTA 3 for Three-Dimensional Visualization of Crystal, Volumetric and Morphology Data. *J Appl Crystallogr* **2011**, *44* (6), 1272–1276. https://doi.org/10.1107/S0021889811038970.

(33) Buschmann, H.; Dölle, J.; Berendts, S.; Kuhn, A.; Bottke, P.; Wilkening, M.; Heitjans, P.; Senyshyn, A.; Ehrenberg, H.; Lotnyk, A.; Duppel, V.; Kienle, L.; Janek, J. Structure and Dynamics of the Fast Lithium Ion Conductor "Li 7La3Zr2O12." *Physical Chemistry Chemical Physics* **2011**, *13* (43), 19378–19392. https://doi.org/10.1039/c1cp22108f.

(34) Kuhn, A.; Choi, J. Y.; Robben, L.; Tietz, F.; Wilkening, M.; Heitjans, P. Li Ion Dynamics in Al-Doped Garnet-Type Li7La3Zr 2O12 Crystallizing with Cubic Symmetry. *Zeitschrift fur Physikalische Chemie* **2012**, *226* (5–6), 525–537. https://doi.org/10.1524/zpch.2012.0250.

(35) Düvel, A.; Kuhn, A.; Robben, L.; Wilkening, M.; Heitjans, P. Mechanosynthesis of Solid Electrolytes: Preparation, Characterization, and Li Ion Transport Properties of Garnet-Type Al-Doped Li 7La 3Zr 2O 12 Crystallizing with Cubic Symmetry. *Journal of Physical Chemistry C* **2012**, *116* (29), 15192–15202. https://doi.org/10.1021/jp301193r.

(36) Rettenwander, D.; Blaha, P.; Laskowski, R.; Schwarz, K.; Bottke, P.; Wilkening, M.; Geiger, C. A.; Amthauer, G. DFT Study of the Role of Al3+ in the Fast Ion-Conductor Li 7-3xAl3+xLa3Zr2O 12 Garnet. *Chemistry of Materials* **2014**, *26* (8), 2617–2623. https://doi.org/10.1021/cm5000999.

(37) Rettenwander, D.; Langer, J.; Schmidt, W.; Arrer, C.; Harris, K. J.; Terskikh, V.; Goward, G. R.; Wilkening, M.; Amthauer, G. Site Occupation of Ga and Al in Stabilized Cubic Li7-3(x + y)GaxAlyLa3Zr2O12 Garnets as Deduced from 27Al and 71Ga MAS NMR at Ultrahigh Magnetic Fields. *Chemistry of Materials* **2015**, *27* (8), 3135–3142. https://doi.org/10.1021/acs.chemmater.5b00684.

(38) Mukhopadhyay, S.; Thompson, T.; Sakamoto, J.; Huq, A.; Wolfenstine, J.; Allen, J. L.; Bernstein, N.; Stewart, D. A.; Johannes, M. D. Structure and Stoichiometry in Supervalent Doped Li7La3Zr2O12. *Chemistry of Materials* **2015**, *27* (10), 3658–3665. https://doi.org/10.1021/acs.chemmater.5b00362.

(39) Chen, Y.; Rangasamy, E.; Liang, C.; An, K. Origin of High Li+ Conduction in Doped Li7La3Zr2O12 Garnets. *Chemistry of Materials* **2015**, *27* (16), 5491–5494. https://doi.org/10.1021/acs.chemmater.5b02521.

(40) Shin, D. O.; Oh, K.; Kim, K. M.; Park, K.-Y.; Lee, B.; Lee, Y.-G.; Kang, K. Synergistic Multi-Doping Effects on the Li7La3Zr2O12 Solid Electrolyte for Fast Lithium Ion Conduction. *Sci Rep* **2015**, *5* (1), 18053. https://doi.org/10.1038/srep18053.

(41) Karasulu, B.; Emge, S. P.; Groh, M. F.; Grey, C. P.; Morris, A. J. Al/Ga-Doped Li7La3Zr2O12 Garnets as Li-Ion Solid-State Battery Electrolytes: Atomistic Insights into Local Coordination Environments and Their Influence on 17O, 27Al, and 71Ga NMR Spectra. *J Am Chem Soc* **2020**, *142* (6), 3132–3148. https://doi.org/10.1021/jacs.9b12685.

(42) Bernuy-Lopez, C.; Manalastas, W.; Lopez Del Amo, J. M.; Aguadero, A.; Aguesse, F.; Kilner, J. A. Atmosphere Controlled Processing of Ga-Substituted Garnets for High

Li-Ion Conductivity Ceramics. *Chemistry of Materials* **2014**, *26* (12), 3610–3617. https://doi.org/10.1021/cm5008069.

(43) Rettenwander, D.; Geiger, C. A.; Tribus, M.; Tropper, P.; Amthauer, G. A Synthesis and Crystal Chemical Study of the Fast Ion Conductor Li 7-3 XGaxLa3 Zr2O12 with x = 0.08 to 0.84. *Inorg Chem* **2014**, *53* (12), 6264–6269. https://doi.org/10.1021/ic500803h.

(44) Jalem, R.; Rushton, M. J. D.; Manalastas, W.; Nakayama, M.; Kasuga, T.; Kilner, J. A.; Grimes, R. W. Effects of Gallium Doping in Garnet-Type Li7La3Zr2O12 Solid Electrolytes. *Chemistry of Materials* **2015**, *27* (8), 2821–2831. https://doi.org/10.1021/cm5045122.

(45) Buannic, L.; Orayech, B.; López Del Amo, J. M.; Carrasco, J.; Katcho, N. A.; Aguesse, F.; Manalastas, W.; Zhang, W.; Kilner, J.; Llordés, A. Dual Substitution Strategy to Enhance Li+ Ionic Conductivity in Li7La3Zr2O12 Solid Electrolyte. *Chemistry of Materials* **2017**, *29* (4), 1769–1778. https://doi.org/10.1021/acs.chemmater.6b05369.

(46) Vema, S.; Sayed, F. N.; Nagendran, S.; Karagoz, B.; Sternemann, C.; Paulus, M.; Held, G.; Grey, C. P. Understanding the Surface Regeneration and Reactivity of Garnet Solid-State Electrolytes. *ACS Energy Lett* **2023**, 3476–3484. https://doi.org/10.1021/acsenergylett.3c01042.

(47) Rodriguez-Carvajal, J. Recent Advances in Magnetic Structure Determination Neutron Powder Diffraction. *Physica B Condens Matter* **1993**, *192* (93), 113. https://doi.org/10.1016/0921-4526(93)90108-I.

(48) Wang, Q.; Hu, B.; Lafon, O.; Trébosc, J.; Deng, F.; Amoureux, J. P. Double-Quantum Homonuclear NMR Correlation Spectroscopy of Quadrupolar Nuclei Subjected to Magic-Angle Spinning and High Magnetic Field. *Journal of Magnetic Resonance* **2009**, *200* (2), 251–260. https://doi.org/10.1016/j.jmr.2009.07.009.

(49) Massiot, D.; Fayon, F.; Capron, M.; King, I.; Le Calvé, S.; Alonso, B.; Durand, J.-O.; Bujoli, B.; Gan, Z.; Hoatson, G. Modelling One- and Two-Dimensional Solid-State NMR Spectra. *Magnetic Resonance in Chemistry* **2002**, *40* (1), 70–76. https://doi.org/10.1002/mrc.984.

(50) Haouas, M.; Taulelle, F.; Martineau, C. Recent Advances in Application of 27Al NMR Spectroscopy to Materials Science. *Prog Nucl Magn Reson Spectrosc* **2016**, *94–95*, 11–36. https://doi.org/10.1016/j.pnmrs.2016.01.003.

(51) El-Shinawi, H.; Paterson, G. W.; MacLaren, D. A.; Cussen, E. J.; Corr, S. A. Low-Temperature Densification of Al-Doped Li7La3Zr2O12: A Reliable and Controllable Synthesis of Fast-Ion Conducting Garnets. *J Mater Chem A Mater* **2017**, *5* (1), 319–329. https://doi.org/10.1039/c6ta06961d.

(52) Zhuang, L.; Huang, X.; Lu, Y.; Tang, J.; Zhou, Y.; Ao, X.; Yang, Y.; Tian, B. Phase Transformation and Grain-Boundary Segregation in Al-Doped Li7La3Zr2O12 Ceramics. *Ceram Int* **2021**, *47* (16), 22768–22775. https://doi.org/10.1016/j.ceramint.2021.04.295.

(53) Sacci, R. L.; McAuliffe, R. D.; Malkowski, T. F.; Kidder, N.; Chen, X. C.; Huq, A.; Kirkham, M.; Armstrong, B. L.; Daemen, L. L.; Veith, G. M. La2Zr2O7Nanoparticle-Mediated Synthesis of Porous Al-Doped Li7La3Zr2O12Garnet. *Inorg Chem* **2021**, *60* (13), 10012–10021. https://doi.org/10.1021/acs.inorgchem.1c01300.

(54) Wang, Z.; Li, T.; Jiang, Y.; Lafon, O.; Liu, Z.; Trébosc, J.; Baiker, A.; Amoureux, J.-P.; Huang, J. Acidity Enhancement through Synergy of Penta- and Tetra-Coordinated Aluminum Species in Amorphous Silica Networks. *Nat Commun* **2020**, *11* (1), 225. https://doi.org/10.1038/s41467-019-13907-7.

(55) Geller, S.; Bala, V. B. Crystallographic Studies of Perovskite-like Compounds. II. Rare Earth Alluminates. *Acta Crystallogr* **1956**, *9* (12), 1019–1025. https://doi.org/10.1107/S0365110X56002965.

(56) Marezio, M. The Crystal Structure and Anomalous Dispersion of γ-LiAlO $_2$. *Acta Crystallogr* **1965**, *19* (3), 396–400. https://doi.org/10.1107/S0365110X65003511.

(57) Schwab, C.; Häuschen, G.; Mann, M.; Roitzheim, C.; Guillon, O.; Fattakhova-Rohlfing, D.; Finsterbusch, M. Towards Economic Processing of High Performance Garnets – Case Study on Zero Li Excess Ga-Substituted LLZO. *J Mater Chem A Mater* **2023**, *11* (11), 5670–5680. https://doi.org/10.1039/D2TA09250F.

(58) Famprikis, T.; Canepa, P.; Dawson, J. A.; Islam, M. S.; Masquelier, C. Fundamentals of Inorganic Solid-State Electrolytes for Batteries. *Nat Mater* **2019**, *18* (12), 1278–1291. https://doi.org/10.1038/s41563-019-0431-3.

(59) Moy, A. C.; Häuschen, G.; Fattakhova-Rohlfing, D.; Wolfenstine, J. B.; Finsterbusch, M.; Sakamoto, J. The Effects of Aluminum Concentration on the Microstructural and Electrochemical Properties of Lithium Lanthanum Zirconium Oxide. *J Mater Chem A Mater* **2022**, *10* (41), 21955–21972. https://doi.org/10.1039/D2TA03676B.

(60) Ash, J. T.; Grandinetti, P. J. Solid-State NMR Characterization of 69Ga and 71Ga in Crystalline Solids. *Magnetic Resonance in Chemistry* **2006**, *44* (9), 823–831. https://doi.org/10.1002/mrc.1841.

(61) Li, J.; Luo, H.; Liu, K.; Zhang, J.; Zhai, H.; Su, X.; Wu, J.; Tang, X.; Tan, G. Excellent Stability of Ga-Doped Garnet Electrolyte against Li Metal Anode *via* Eliminating LiGaO $_2$ Precipitates for Advanced All-Solid-State Batteries. *ACS Appl Mater Interfaces* **2023**, *15* (5), 7165–7174. https://doi.org/10.1021/acsami.2c21603.

(62) Uitz, M.; Epp, V.; Bottke, P.; Wilkening, M. Ion Dynamics in Solid Electrolytes for Lithium Batteries: Probing Jump Rates and Activation Energies through Time-Domain Li NMR. *J Electroceram* **2017**, *38* (2–4), 142–156. https://doi.org/10.1007/s10832-017-0071-4.

Table of Contents graphic